Chemical
Science

ROYAL SOCIETY OF CHEMISTRY

EDGE ARTICLE

View Article Online
View Journal | View Issue

Check for updates

Cite this: *Chem. Sci.*, 2024, **15**, 11480

All publication charges for this article have been paid for by the Royal Society of Chemistry

Received 16th April 2024
Accepted 18th June 2024

DOI: 10.1039/d4sc02506g

rsc.li/chemical-science

An integrated "rigid–flexible" strategy by side chain engineering towards high ion-conduction cationic covalent organic framework electrolytes†

Jian Song, Li Lin, Fengchao Cui, Heng-Guo Wang, * Yuyang Tian *
and Guangshan Zhu

In recent years, solid-state lithium metal batteries (SSLMBs) have become a new development trend, and it has become a top priority to design solid-state electrolytes (SSEs) that can rapidly and stably transport lithium ions in a variety of climatic environments. In this work, an integrated "rigid–flexible" dual-functional strategy is proposed to develop a cationic covalent organic framework (EO-BIm-iCOF) with well-defined flexible oligo(ethylene oxide) (EO) chains as an SSE for SSLMBs. As expected, the synergistic effects of the rigid cationic framework and flexible EO chains not only promote the dissociation of LiTFSI salts, but also greatly improve the transport of lithium ions, which endows LITFSI@EO-BIm-iCOF SSEs with a high Li^+ conductivity of 1.08×10^{-4} S cm^{-1} and ionic transference number of 0.69 at room temperature. Besides, the molecular dynamics (MD) simulations have also elucidated the diffusion and transport mechanism of lithium ions in LITFSI@EO-BIm-iCOF SSEs. Interestingly, the assembled SSLMBs wherein $LiFePO_4$ is paired with LITFSI@EO-BIm-iCOF SSEs display decent electrochemical properties at higher and lower temperatures. This work provides a great development prospect for the application of cationic COFs in solid-state batteries.

Introduction

With the growing needs of high-energy-density and high-safety rechargeable batteries, solid-state lithium metal batteries (SSLMBs) have emerged.[1–4] Different from the conventional lithium ion batteries, SSLMBs use lithium metal and solid-state electrolytes (SSEs) to replace the graphite anode and organic liquid electrolytes, respectively, thus resulting in high energy density and high safety.[5–10] Therefore, research in the field of SSLMBs concentrates mainly on the development of SSEs and the construction of compatible interfaces between the cathode and anode. Solid polymer electrolytes (SPEs), typically poly(ethylene oxide) (PEO), poly(methyl methacrylate) (PMMA) and poly(vinyl alcohol) (PVA), have been investigated widely.[11–17] Their excellent processability, low cost, and tunable interfacial compatibility provide opportunities for the realization of SSLMBs. Unfortunately, the poor ion conductivity at ambient temperature ($<10^{-4}$ S cm^{-1}), lower cation transference number (0.2–0.4), and oxidative decomposition at high potentials of SPEs seriously prohibit their further application.[5,18,19] Therefore, exploiting SSEs with fast ion transport ability remains highly challenging in achieving high performance SSLMBs.

Covalent organic frameworks (COFs) are a class of rapidly developing crystalline porous polymers, which have been applied in many fields such as adsorption, separation, catalysis, sensing, energy storage and conversion.[20–26] The high-porosity structure and well-tailored channels of COFs could accommodate ions and offer a continuous transportation pathway.[27–33] Recently, a few COFs have been successfully demonstrated to be lithium ion conductors and promisingly used as SSEs in the SSLMBs.[29–41] However, most of the COFs still exhibit low ion conductivity and cation transference number at ambient temperature, which may lead to the problems of inadequate long cycle performances and out of operation at lower temperatures for solid-state batteries. One critical problem in constructing advanced SSEs is the need to accelerate the effective dissociation of ion pairs and promote the ion migration at room temperature. Note that the free movement of the anions could cause concentration polarization and dendritic growth, thus accelerating the deterioration of lithium metal anodes.[42–44] In this context, single-ion conducting SSEs are developed by decorating anions on the COF backbone, which can address the issues caused by anion migration.[33,36,37] In addition, incorporation of flexible functional side chains in COFs could give rise to strong lithium ion binding ability and flexible motion characteristics, which can not only promote the dissociation of lithium salts, but also provide rich and flexible jumping sites for

---

Key Laboratory of Polyoxometalate and Reticular Material Chemistry of Ministry of Education, Faculty of Chemistry, Northeast Normal University, Changchun 130024, China. E-mail: wanghg061@nenu.edu.cn; tianyy100@nenu.edu.cn

† Electronic supplementary information (ESI) available. See DOI: https://doi.org/10.1039/d4sc02506g

lithium ions inside the channels during the transport process.[31,32,39,40] The currently reported COFs either utilize binding sites on the skeleton or perform ion conduction through functional side chains in the channel, however, simultaneously utilizing the functional features of both the skeleton and the channel side chains to transport ions has been less mentioned.

Herein, we propose an integrated "rigid–flexible" dual-functional strategy (Fig. 1a), that is, to design and construct a rigid cationic COF skeleton, while uniformly introducing functional flexible segments capable of transporting lithium ions through side chain engineering. As a proof of concept, we designed and synthesized a two-dimensional mesoporous COF, named BIm-COF, by intentionally selecting 4,4′,4″,4‴-(ethene-1,1,2,2-tetrayl)tetraaniline (ETTA) and 4,4′-(1-methyl-1*H*-benzo[*d*]imidazole-4,7-diyl) dibenzaldehyde (BImDB). By one-step post modification, dual-functionalization including both the construction of cationization skeletons and the introduction of flexible oligo(ethylene oxide) (EO) chains in the pores of cationic COF has been achieved simultaneously, denoted as EO-BIm-iCOF (Fig. 1b). Interestingly, the rigid cationic framework traps anions by the coulombic interaction and the flexible EO chains bind and transfer lithium ions through the segment motion of chains, resulting in rigid–flexible cooperation that promotes the efficient dissociation of lithium salts and fast transport of lithium ions in the channels. As expected, the LITFSI@EO-BIm-iCOF has a wide electrochemical window (4.65 V *vs.* Li$^+$/Li), higher lithium-ion conductivity ($\sigma = 1.08 \times 10^{-4}$ S cm^{-1} at 25 °C) and transference number ($t_{\mathrm{Li}^+} = 0.69$) than the original BIm-COF. Theoretical calculations further show that LITFSI@EO-BIm-iCOF has a higher diffusion and transport efficiency of lithium ions. Moreover, the assembled SSLMBs wherein LiFePO$_4$ (LFP) is paired with the LITFSI@EO-BIm-iCOF solid electrolyte display decent electrochemical properties in

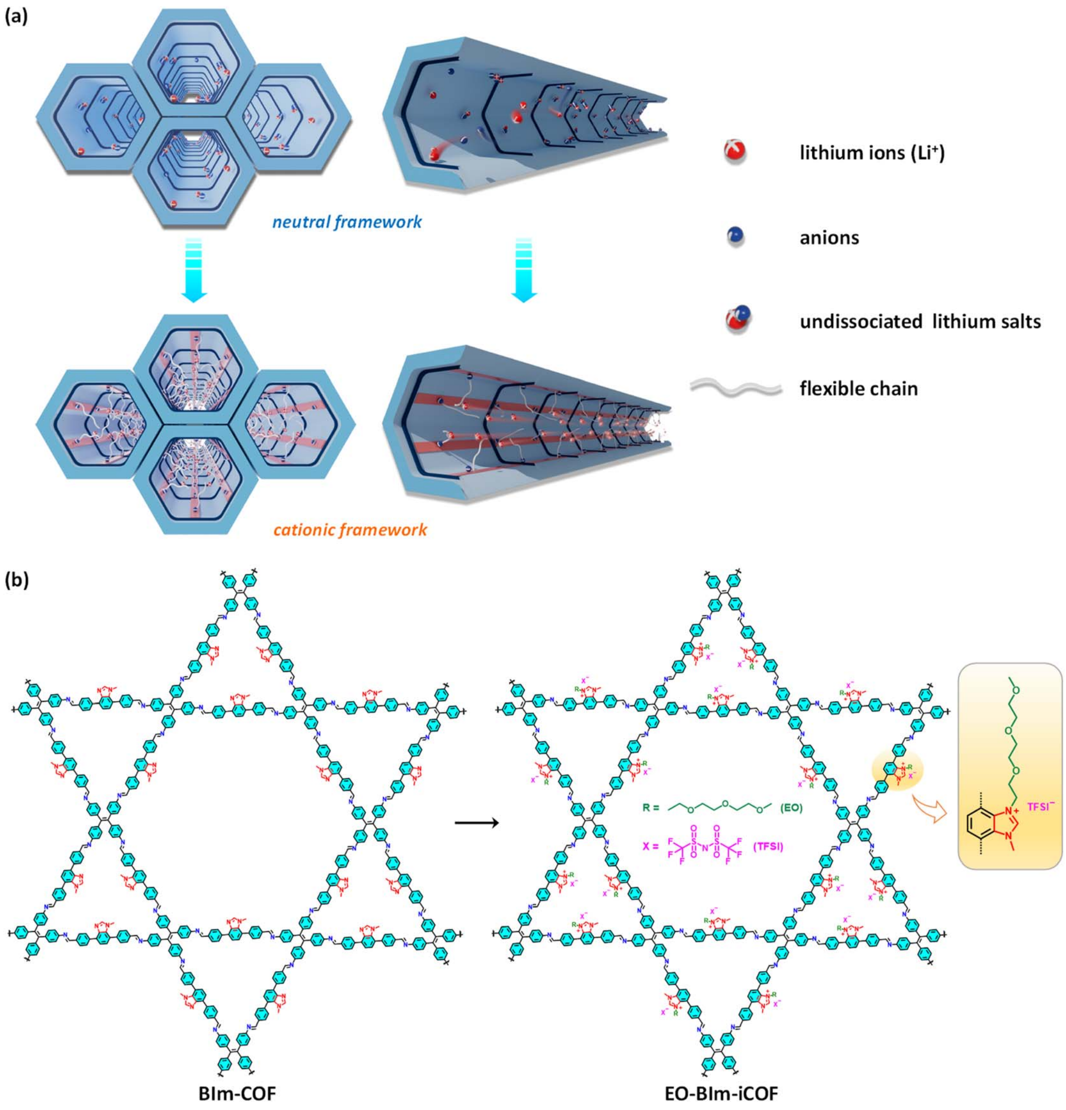

Fig. 1 (a) Schematic illustration of the lithium ion transport process in COFs with the traditional bare channels and integrated "rigid–flexible" strategy, respectively. (b) Synthetic scheme of the two-dimensional mesoporous BIm-COF and post-modified EO-BIm-iCOF, respectively.

a wide temperature range. This strategy can also be applied to other porous materials, providing a feasible method and theoretical basis for the design of SSEs.

Results and discussion

Material synthesis and characterization

BIm-COF was synthesized under solvothermal conditions at 120 °C for 3 days. Subsequently, we referred to the synthesis conditions of methylimidazole ionic liquids and used the methylimidazole groups on the COF skeleton for post-modification. To ensure the success of post-modification, we first optimized experimental conditions using 1-methylbenzimidazole as a model compound (Fig. S1†). Finally, the target product EO-BIm-iCOF was obtained by replacing Br^- ions with bis(trifluoromethylsulfonyl)imide ($TFSI^-$) anions through the ion exchange method. The chemical structures of as-synthesized BIm-COF and post-modified EO-BIm-iCOF were characterized using Fourier transform infrared (FT-IR) spectroscopy. The appearance of a new C=N stretching vibration band around 1620 cm^{-1} confirms the successful formation of imine linkages for COFs (Fig. S2†). EO-BIm-iCOF shows the characteristic C–O–C stretching vibrations at 1100 cm^{-1} and 1060 cm^{-1}, and $-CH_3$ and $-CH_2$ stretching vibrations at 2930 cm^{-1} and 2875 cm^{-1}, respectively, which are derived from EO chains. Furthermore, the stretching bands at 1350 cm^{-1} and 1130 cm^{-1} correspond to the $-SO_2$, the bands at 1226 cm^{-1}, 1194 cm^{-1} and 740 cm^{-1} should correspond to the stretching and bending vibrations of $-CF_3$ from the exchanged $TFSI^-$ anions.[45]

The powder X-ray diffraction (PXRD) experiment and theoretical structural simulation have been performed to determine the crystalline structure of the as-synthesized BIm-COF. The experimental PXRD patterns (Fig. 2a) of BIm-COF exhibit a set of intense peaks at $2\theta = 1.90°$, 3.28°, 3.80°, 5.71°, 7.58°, 9.54° and 20.0°, which are assigned to the Bragg diffraction of (100), (110), (200), (300), (400), (330) and (001) planes, respectively. Structural models based on the eclipsed (AA) and staggered (AB) stacking conformations with the *kgm* topology were built and optimized by using Materials Studio (Fig. 2b and S3–S4†). The experimental data well match the simulated PXRD patterns of the AA stacking model ($a = 50.85$ Å, $b = 56.07$ Å, $c = 4.53$ Å, $\alpha = \beta = 90°$, and $\gamma = 120°$ with the factors of $R_p = 3.93\%$ and $R_{wp} = 5.67\%$ according to Pawley refinement). Furthermore, the transmission electron microscopy (TEM) image demonstrates that BIm-COF has a long-range ordered highly crystalline structure. In the high-resolution TEM (HR-TEM) image and inverse fast Fourier transform of HR-TEM (IFFT-HR-TEM) image, numerous continuous hexagonal channels have been clearly observed, which basically match the simulated AA stacking structure of BIm-COF along the [001] direction (Fig. 2c–e and S5†). For post-modified EO-BIm-iCOF, the crystallinity is greatly diminished from PXRD patterns since abundant EO chains and more bulky $TFSI^-$ anions are introduced,[41] and no obvious lattice fringes are observed in TEM images (Fig. S6 and S7†).

Permanent porosities of BIm-COF and EO-BIm-iCOF were measured by nitrogen sorption isotherms at 77 K. As shown in Fig. 2f, BIm-COF displays a typical combination of type I and type IV isotherms, indicating the coexistence of micropores and mesopores in the as-synthesized COF. The Brunauer–Emmett–Teller (BET) surface area is calculated to be 256 $m^2\ g^{-1}$ with the total pore volume of 0.34 $cm^3\ g^{-1}$. The low surface area may be attributed to the presence of a small amount of oligomers within the pores, or the local structure is defective. Furthermore, the existence of large methylimidazole groups on the side wall of the material structure will also reduce the specific surface area to a certain extent.[46–48] According to the calculation of Quenched Solid Density Functional Theory (QSDFT) equilibrium model, the pore size distribution of BIm-COF is mainly at 13.0 Å, 19.0 Å, and 34.0 Å, respectively, which is well in agreement with the three theoretical pore sizes of ∼11.0 Å, 16.0 Å, and 37.0 Å deduced from the AA stacking model (Fig. 2g). In addition, the nitrogen sorption isotherm of EO-BIm-iCOF shows an extremely low BET surface area of 30 $m^2\ g^{-1}$ (Fig. S8†), suggesting that a large number of EO chains and TFSI anions have successfully modified and occupied the pores of COF. Elemental analyses, solid-state ^{13}C cross-polarization magic angle spinning nuclear magnetic resonance (CP/MAS NMR), and X-ray photoelectron spectroscopy (XPS) were also utilized to demonstrate the successful modification of the flexible EO chains and complete anion exchange (details in the ESI, Fig. S9 and S10†). Scanning electron microscopy (SEM) shows that both BIm-COF and EO-BIm-iCOF exhibit the small block morphology (Fig. S11†). TEM image and the corresponding elemental maps clearly demonstrate the homogeneous distribution of C, N, O, S and F throughout EO-BIm-iCOF (Fig. 2h), revealing the uniform introduction of EO chains and TFSI anions in the COF. Thermogravimetric analysis (TGA) further reveals that BIm-COF and EO-BIm-iCOF possess good thermal stability up to 200 °C under an air atmosphere (Fig. S12†). The stability study of the materials has been conducted *via* PXRD. The results show that BIm-COF maintains the crystallinity and stability after 100 °C heat treatment (Fig. S13†).

Lithium ion conduction properties

The ion conductivities (σ) of LITFSI@COFs were measured based on the electrochemical impedance spectroscopy (EIS) of stainless steel‖LITFSI@COFs‖stainless steel symmetric cells. According to the Nyquist plots (Fig. 3a), LITFSI@EO-BIm-iCOF exhibits a high ion conductivity of 1.08×10^{-4} S cm^{-1} at 25 °C, much higher than the pristine LITFSI@BIm-COF of 2.98×10^{-6} S cm^{-1} (Fig. S16†). The Li^+ ion conducting activation energies (E_a) were calculated through a set of Nyquist plots measured at various temperatures ranging from 25 °C to 85 °C. As shown in Fig. 3b, the activation energy of LITFSI@EO-BIm-iCOF is 0.19 eV from the linear Arrhenius plot, which is lower than 0.25 eV of LITFSI@BIm-COF (Fig. S17†), indicating the low energy barrier for Li^+ transport in LITFSI@EO-BIm-iCOF. This is mainly attributed to the continuous flexible EO chains modified in the channels as lithium ion hopping sites, promoting the dissociation of lithium salts, and forming the continuous ion transport pathways in the LITFSI@EO-BIm-iCOF.

The Li^+ transference numbers (t_{Li^+}) of LITFSI@COFs were tested by direct current (DC) polarization and alternating

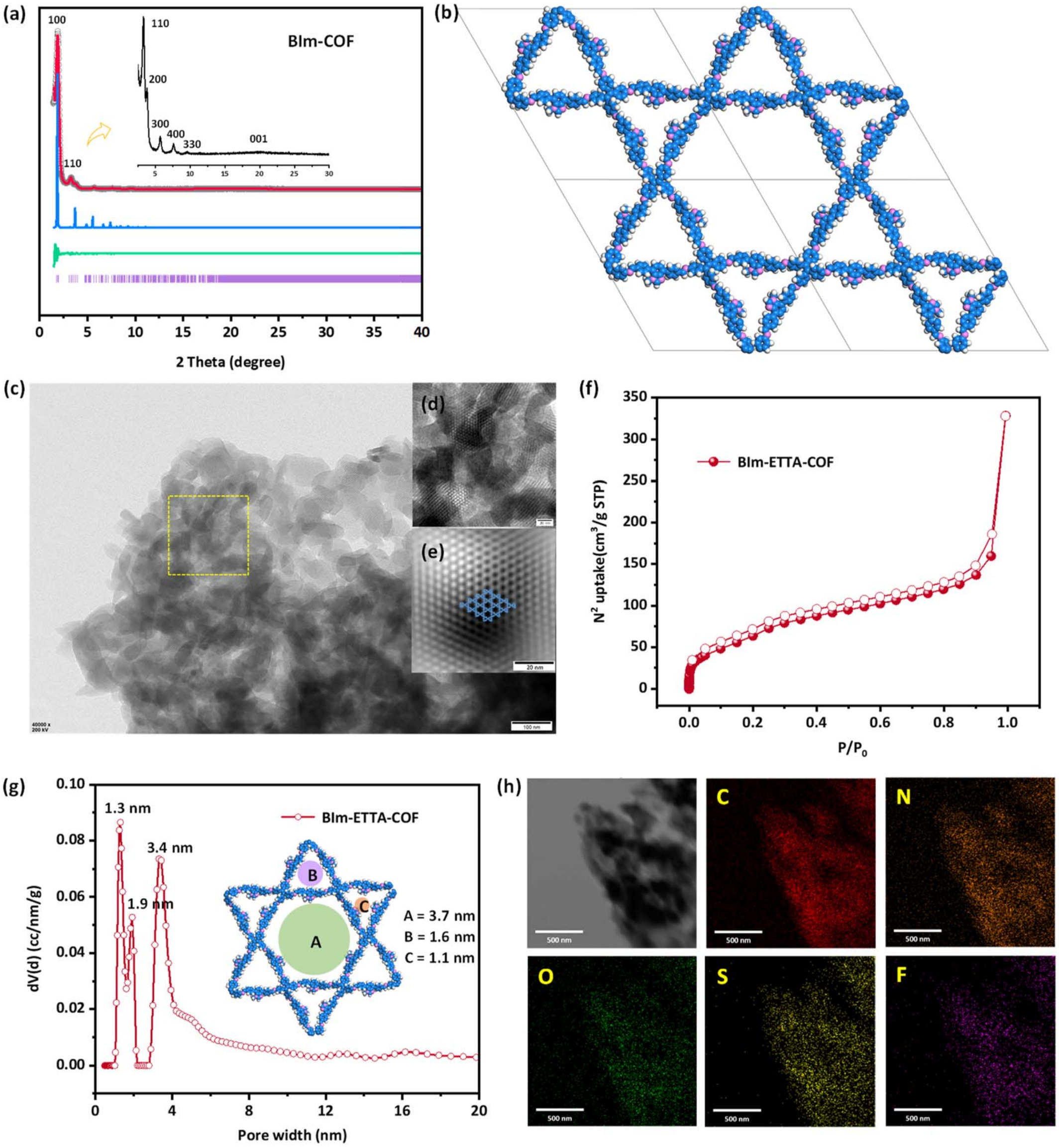

Fig. 2 (a) PXRD patterns of as-synthesized BIm-COF and the corresponding AA stacking structure, experimental (black), refined (red), their difference plot (green), simulated (blue), and the positions of the Bragg reflections (purple). The inset shows enlarged experimental PXRD patterns. (b) Crystal structure of BIm-COF in AA-stacking mode. (c) TEM images of BIm-COF, inset: HRTEM images (d), and IFFT-HR-TEM images and the matched AA stacking structure (e). (f) N_2 adsorption (filled symbol) and desorption (open symbols) isotherm curves of as-synthesized BIm-COF measured at 77 K. (g) Pore-size distribution profile of BIm-COF accorded with the structural theoretical pore size. (h) TEM and EDS mapping images of post-modified EO-BIm-iCOF.

current (AC) impedance measurements of Li‖LITFSI@COFs‖Li symmetric cells at room temperature. According to the Bruce–Vincent–Evans (BVE) technique, the Li^+ transference number of LITFSI@EO-BIm-iCOF can be calculated as 0.69 (Fig. 3c), which is higher than that of LITFSI@BIm-COF ($t_{Li^+} = 0.41$) (Fig. S18†) and traditional PEO-based SPEs ($t_{Li^+} < 0.2$).[49] This result further illustrates that the positively charged framework and flexible EO chains immobilized in channels can efficiently dissociate the lithium salts and trap the anions to accelerate the transport of Li^+ in LITFSI@EO-BIm-iCOF. Moreover, the electrochemical stability of LITFSI@COFs was investigated by performing linear sweep voltammetry (LSV) at a sweep rate of 1 mV s^{-1} at room temperature. The LSV graphs suggest that both LITFSI@EO-BIm-iCOF and LITFSI@BIm-COF possess a wide window of electrochemical stability, wherein no significant current flow corresponding to electrolyte decomposition is observed up to 4.65 V and 5.35 V, respectively (Fig. 3d and S19†). Compared to traditional PEO-based polymer electrolytes,[50–53] the higher stability of EO chains is attributed to the shielding of porous frameworks. The ultrahigh electrochemical stability of LITFSI@EO-BIm-iCOF as the SSEs allows reversible operation in cooperation with the Li-metal anode and high-voltage cathodes for high energy density LMBs. Furthermore, the symmetrical Li‖LITFSI@EO-BIm-iCOF‖Li cell has also been assembled for the constant current electrochemical plating/stripping cycle test at 30 °C and the current density was 0.25 mA cm^{-2} to investigate

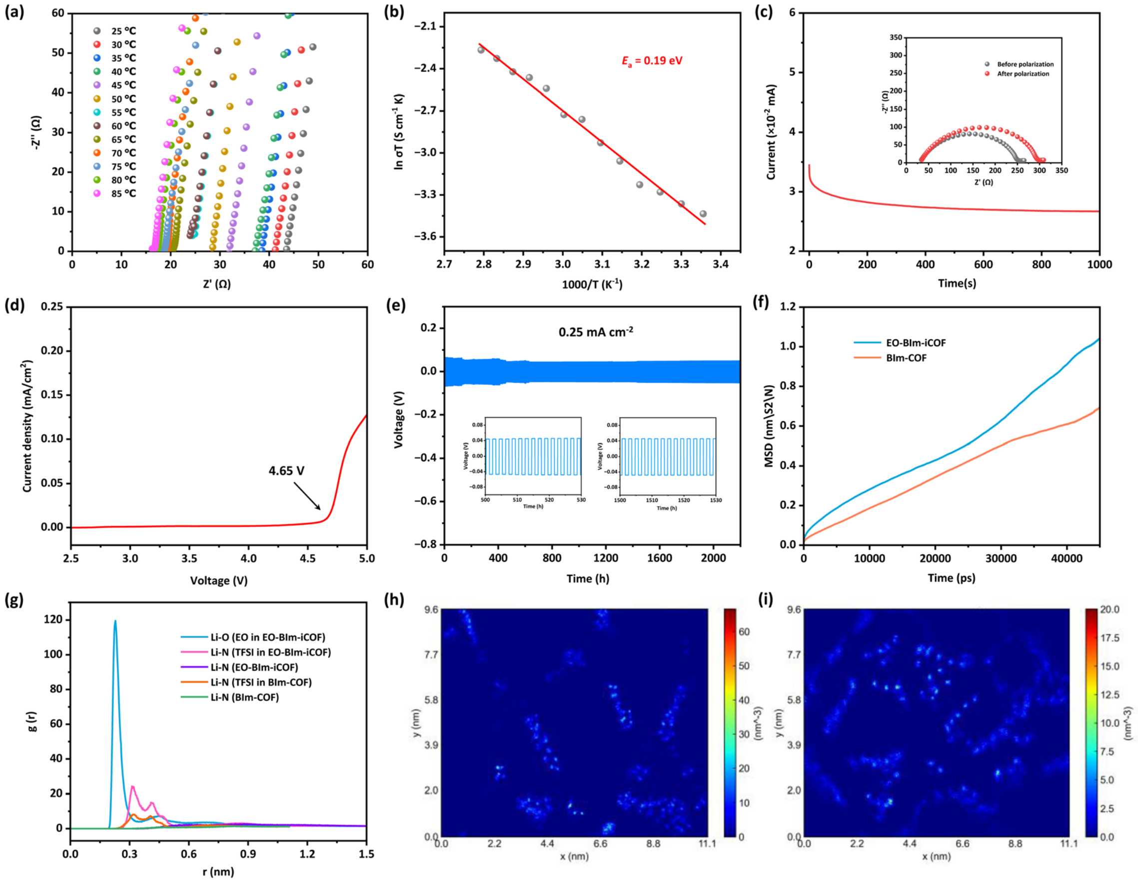

Fig. 3 (a) The EIS spectra and (b) Arrhenius plots of LITFSI@EO-BIm-iCOF at 25 °C to 85 °C. (c) Chronoamperometry curves of a Li||LITFSI@EO-BIm-iCOF||Li symmetric cell under 10 mV polarization at room temperature. Inset: EIS spectra before and after polarization, respectively. (d) LSV curve of LITFSI@EO-BIm-iCOF. (e) Li plating/stripping test of the Li||LITFSI@EO-BIm-iCOF||Li symmetric cell at 0.25 mA cm^{-2}. (f) MSD of Li$^+$ in LITFSI@EO-BIm-iCOF and LITFSI@BIm-COF. (g) RDF of LITFSI@EO-BIm-iCOF and LITFSI@BIm-COF. (h) Li$^+$ number density of LITFSI@BIm-COF. (i) Li$^+$ number density of LITFSI@EO-BIm-iCOF.

the stability of the interface between the lithium foil and the LITFSI@EO-BIm-iCOF electrolyte. As observed in Fig. 3e, the Li||LITFSI@EO-BIm-iCOF||Li cell shows a stable plateau after plating/stripping for 2200 h under stable voltage polarization. This indicates that the LITFSI@EO-BIm-iCOF can alleviate the concentration polarization generated during the charge–discharge processes of the battery, and effectively reduce the generation of lithium dendrites to improve the stability and safety of the SSLMBs.

Mechanism study of lithium ion conduction

The ^{7}Li solid-state NMR spectra have been tested to further study the local chemical environments and dynamics of Li$^+$ ions in pure LiTFSI salts, LiTFSI@BIm-COF, and LiTFSI@EO-BIm-iCOF. As shown in Fig. S20,† the Li$^+$ ions in the pure LiTFSI salt are in a strongly bound state and appear in a high field state (−0.18 ppm) due to the large number of electrons formed near the Li$^+$ ions. By contrast, the chemical shift of LiTFSI@BIm-COF and LiTFSI@EO-BIm-iCOF drastically changes to the lower field state (0.46 ppm and 0.40 ppm, respectively), which generally means that Li$^+$ ions are dissociated from the LiTFSI salts.[34,54] Moreover, a slight upfield shift in LiTFSI@EO-BIm-iCOF indicates a stronger binding ability between Li$^+$ ions and EO chains. The XPS spectra of pure LiTFSI, LiTFSI@BIm-COF, and LiTFSI@EO-BIm-iCOF also show that the binding energy peak of Li 1 s changes to a certain extent from 56.5 eV to 56.1 eV and 56.3 eV, respectively (Fig. S21†), indicating the existence of the interaction. To bring a better insight into the high Li$^+$ ion conductivity and transference number of the LITFSI@EO-BIm-iCOF material as an SSE for SSLMBs, the molecular dynamics (MD) simulations of LITFSI@BIm-COF and post-modified LITFSI@EO-BIm-iCOF were performed to understand the diffusion dynamics of lithium ions. Theoretical stimulation snapshot (Fig. S22†) results show that the diffusion of Li$^+$ in LITFSI@EO-BIm-iCOF is remarkably faster than that in LITFSI@BIm-COF. Moreover, the mean-squared displacement (MSD) was carried out to simulate the quantitative characterization of lithium-ion mobility during the transport process. As shown in Fig. 3f, LITFSI@EO-BIm-iCOF exhibits a higher diffusion coefficient ($D_{\mathrm{Li}^+} = 3.5 \times 10^{-8}$ cm^2 s^{-1}), surpassing the one of LITFSI@BIm-COF ($D_{\mathrm{Li}^+} = 2.4 \times 10^{-8}$ cm^2 s^{-1}), which is consistent with the high Li$^+$ conductivity of LITFSI@EO-BIm-iCOF. This MSD result should be attributed to the synergistic effect of the introduction of flexible EO chains and the cationization of skeletons. The radial distribution function (RDF) results show a dominant peak of Li–O (EO) at 2.3 Å (Fig. 3g), indicating a very strong interaction of Li^+ with EO chains in LITFSI@EO-BIm-iCOF, which significantly exceeds those of Li^+ with $TFSI^-$ anions and COF skeletons. It further reveals that the flexible EO chains can indeed enhance Li^+ dissociation and transport in LITFSI@EO-BIm-iCOF. In addition, we also simulated the Li^+ number density of the two COF materials. The results show that the density distribution of Li^+ LITFSI@BIm-COF (Fig. 3h) is relatively concentrated and mainly distributed near the COF skeleton, while the distribution in LITFSI@EO-BIm-iCOF (Fig. 3i) is relatively loose, indicating that Li^+ in LITFSI@EO-BIm-iCOF diffuses faster and has a wider diffusion range. This is mainly due to the segment motion and ion transport of abundant EO chains inside the COF channels, so that lithium ions are not bound around the skeleton. The above MD calculation results fully show that the introduction of EO flexible chains significantly improves the lithium ion transport efficiency of COF as the solid electrolyte, which is also the key to the smooth transport of lithium ions in a low temperature environment, and further verifies the feasibility of the integrated rigid–flexible strategy in the design of SSEs.

Assembly and testing of solid-state $LiFePO_4$||LITFSI@EO-BIm-iCOF||Li cells

Encouraged by the above-mentioned results, LFP||LITFSI@EO-BIm-iCOF||Li cells were assembled to prove the actual operation performances of LITFSI@COFs as the SSEs. As shown in Fig. 4a and b, the SSLMB based LITFSI@EO-BIm-iCOF exhibits

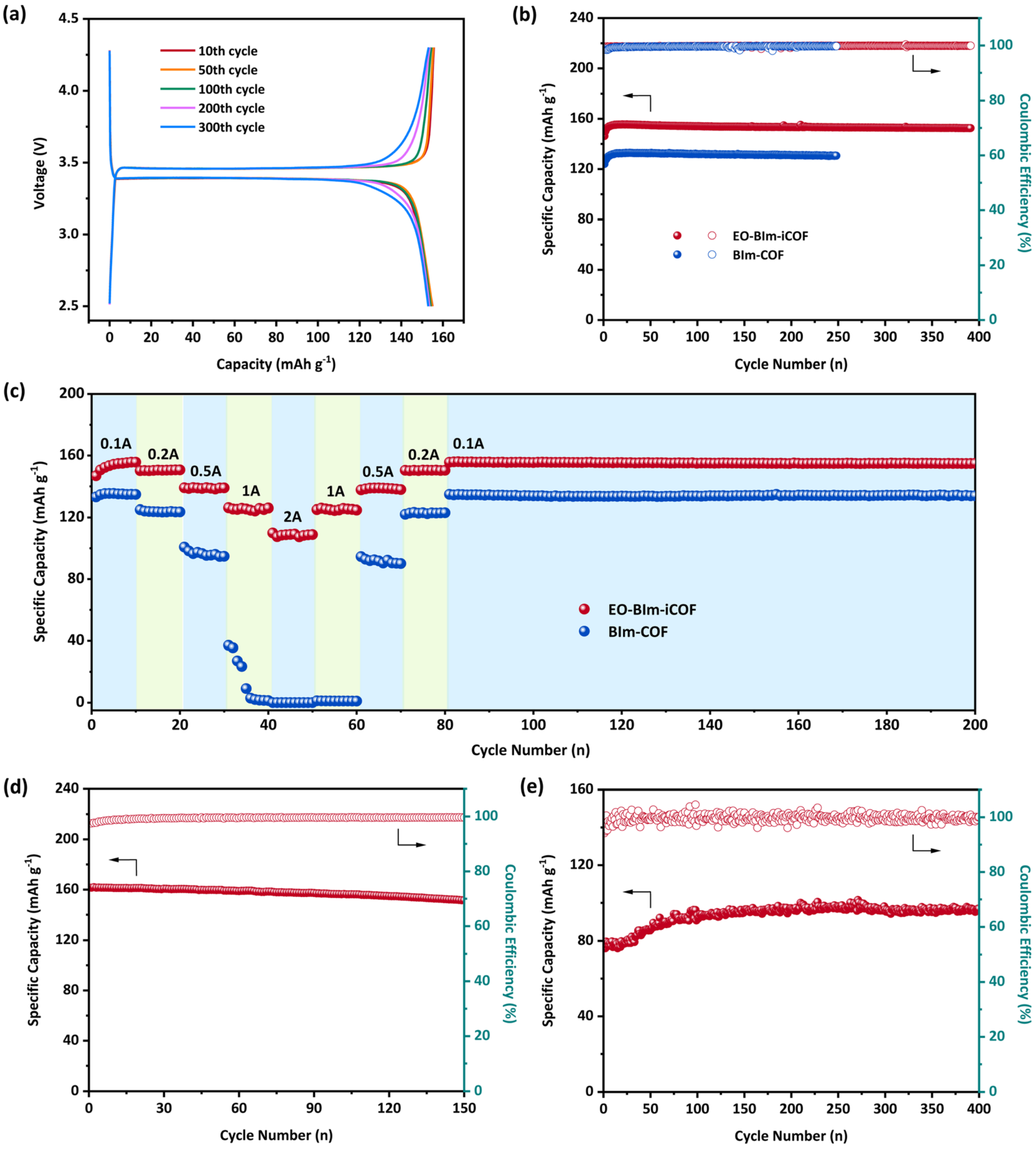

Fig. 4 (a) The voltage profiles, (b) cycling stability and coulombic efficiency of the LFP||LITFSI@EO-BIm-iCOF||Li cell at 100 mA g^{-1}. (c) Rate capabilities of the LFP||LITFSI@COFs||Li cells. (d) Cycling stability and coulombic efficiency of the LFP||LITFSI@EO-BIm-iCOF||Li cell at 100 mA g^{-1} at 60 °C. (e) Cycling stability and coulombic efficiency of the LFP||LITFSI@EO-BIm-iCOF||Li cell at 50 mA g^{-1} at −10 °C.

excellent cycling performance with a high specific capacity of 156 mA h g^{-1} at 100 mA g^{-1} and a capacity retention of 98.8% for over 400 cycles, respectively. The Coulomb efficiencies are kept close to 100%. A higher specific capacity of 164 mA h g^{-1} can be observed at 50 mA g^{-1} at 30 °C (Fig. S23†). The power density of LFP‖LITFSI@EO-BIm-iCOF‖Li cell is shown in Table S1.†[55] The rate performance is also investigated at different current densities of 100 mA g^{-1}, 200 mA g^{-1}, 500 mA g^{-1}, 1 A g^{-1}, and 2 A g^{-1}, respectively. Fig. 4c shows that LITFSI@EO-BIm-iCOF exhibits a more robust rate performance than as-synthesized LITFSI@BIm-COF, which can still run smoothly under the high current density of 2 A g^{-1}. In order to further investigate the potential application of LITFSI@EO-BIm-iCOF as the SSE under a variety of climatic temperatures, we tested the cycling performances of the battery at high and low temperatures, respectively. The excellent cycling performance shows that the battery can still operate smoothly and maintain the high battery specific capacities of 162 mA h g^{-1} at 60 °C and 100 mA h g^{-1} at −10 °C, respectively (Fig. 4d and e). Surprisingly, the battery can still run smoothly for over 500 cycles while placed in the extremely cold climate of −40 °C (Fig. S24†). It shows that LITFSI@EO-BIm-iCOF SSEs has a very good application prospect. At the same time, the feasibility of this integrated “rigid–flexible” strategy for the construction of efficient and stable lithium ion transport path has been fully verified.

Conclusions

In summary, an integrated “rigid–flexible” dual-functional strategy is proposed and proved according to the well-designed LITFSI@EO-BIm-iCOF SSE that consists of the rigid cationic COF skeleton and functional flexible segments. The as-prepared LITFSI@EO-BIm-iCOF SSE exhibits higher ion conductivity (1.08×10^{-4} S cm^{-1}) and Li^+ transference number (0.69) as well as ultrahigh electrochemical stability than its LITFSI@BIm-COF SSE counterpart. Theoretical calculations also indicate that the introduction of the EO chain into the rigid cationic COF skeleton greatly promotes the smooth and fast transport of lithium ions. Moreover, SSLMBs assembled with the LITFSI@EO-BIm-iCOF SSEs show excellent long cycling and rate performances with a capacity of up to 164 mA h g^{-1}. Inspiringly, it also operates smoothly and maintains satisfactory performances at 60 °C and at −10 °C, respectively. This fully demonstrates the feasibility of the rigid-flexible dual-functional strategy for SSEs, which will further promote the development of COFs and other porous framework SSEs for SSLMBs.

Data availability

The data supporting this article have been included as part of the ESI.†

Author contributions

J. S. conducted the experiments with support from H.-G. W., Y. T., and G. Z.; J. S., L. L., and F. C. analyzed the data; J. S. visualized the data; J. S. wrote the article with support from all authors; J. S., H.-G. W., Y. T., and G. Z. designed the research; and G. Z. supervised the project.

Conflicts of interest

There are no conflicts to declare.

Acknowledgements

This work is financially supported by the National Natural Science Foundation of China (Grant No. U21A20330 and 22131004), National Key R&D Program of China (2022YFB3805900), the ‘111’ project (Grant No. B18012), China Postdoctoral Science Foundation (2023M740577), Science and Technology Development Plan Project of Jilin Province, China (20240602105RC), Fundamental Research Funds for the Central Universities (2412023QD013), and Postdoctoral Funding Project of Jilin Province, China.

References

1 M. J. Lee, J. Han, K. Lee, Y. J. Lee, B. G. Kim, K.-N. Jung, B. J. Kim and S. W. Lee, *Nature*, 2022, **601**, 217.
2 Y. Liu, D. Lin, Y. Jin, K. Liu, X. Tao, Q. Zhang, X. Zhang and Y. Cui, *Sci. Adv.*, 2017, **3**, eaao0713.
3 C. Wang, J. Liang, Y. Zhao, M. Zheng, X. Lia and X. Sun, *Energy Environ. Sci.*, 2021, **14**, 2577.
4 C. Yang, Q. Wu, W. Xie, X. Zhang, A. Brozena, J. Zheng, M. N. Garaga, B. H. Ko, Y. Mao, S. He, Y. Gao, P. Wang, M. Tyagi, F. Jiao, R. Briber, P. Albertus, C. Wang, S. Greenbaum, Y.-Y. Hu, A. Isogai, M. Winter, K. Xu, Y. Qi and L. Hu, *Nature*, 2021, **598**, 590.
5 Q. Zhao, S. Stalin, C.-Z. Zhao and L. A. Archer, *Nat. Rev. Mater.*, 2020, **5**, 229.
6 T. Famprikis, P. Canepa, J. A. Dawson, M. S. Islam and C. Masquelier, *Nat. Mater.*, 2019, **18**, 1278.
7 X. Wang, R. Kerr, F. Chen, N. Goujon, J. M. Pringle, D. Mecerreyes, M. Forsyth and P. C. Howlett, *Adv. Mater.*, 2020, **32**, 1905219.
8 B. Xu, X. Li, C. Yang, Y. Li, N. S. Grundish, P.-H. Chien, K. Dong, I. Manke, R. Fang, N. Wu, H. Xu, A. Dolocan and J. B. Goodenough, *J. Am. Chem. Soc.*, 2021, **143**, 6542.
9 J. Zou, A. Trewin, T. Ben and S. Qiu, *Angew. Chem., Int. Ed.*, 2020, **59**, 769.
10 X.-X. Wang, L.-N. Song, L.-J. Zheng, D.-H. Guan, C.-L. Miao, J.-X. Li, J.-Y. Li and J.-J. Xu, *Angew. Chem., Int. Ed.*, 2023, **62**, e202308837.
11 J. Lopez, D. G. Mackanic, Y. Cui and Z. Bao, *Nat. Rev. Mater.*, 2019, **4**, 312.
12 Z. Li, H. Zhang, X. Sun and Y. Yang, *ACS Energy Lett.*, 2020, **5**, 3244.
13 M. Liu, S. Zhang, E. R. H. van Eck, C. Wang, S. Ganapathy and M. Wagemaker, *Nat. Nanotechnol.*, 2022, **17**, 959.
14 X. Wang, C. Zhang, M. Sawczyk, J. Sun, Q. Yuan, F. Chen, T. C. Mendes, P. C. Howlett, C. Fu, Y. Wang, X. Tan,

D. J. Searles, P. Král, C. J. Hawker, A. K. Whittaker and M. Forsyth, *Nat. Mater.*, 2022, **21**, 1057.
15 R. Khurana, J. L. Schaefer, L. A. Archer and G. W. Coates, *J. Am. Chem. Soc.*, 2014, **136**, 7395.
16 X. Zhang, Z. Guo, X. Li, Q. Liu, H. Hu, F. Li, Q. Huang, L. Zhang, Y. Tang and J. Huang, *Energy Environ. Sci.*, 2024, **17**, 1436.
17 Q. Ma, H. Zhang, C. Zhou, L. Zheng, P. Cheng, J. Nie, W. Feng, Y.-S. Hu, H. Li, X. Huang, L. Chen, M. Armand and Z. Zhou, *Angew. Chem., Int. Ed.*, 2016, **55**, 2521.
18 K. Xu, *Chem. Rev.*, 2004, **104**, 4303.
19 Y. Su, X. Rong, A. Gao, Y. Liu, J. Li, M. Mao, X. Qi, G. Chai, Q. Zhang, L. Suo, L. Gu, H. Li, X. Huang, L. Chen, B. Liu and Y.-S. Hu, *Nat. Commun.*, 2022, **13**, 4181.
20 C. S. Diercks and O. M. Yaghi, *Science*, 2017, **355**, eaal1585.
21 T. Ma, E. A. Kapustin, S. X. Yin, L. Liang, Z. Zhou, J. Niu, L.-H. Li, Y. Wang, J. Su, J. Li, X. Wang, W. D. Wang, W. Wang, J. Sun and O. M. Yaghi, *Science*, 2018, **361**, 48.
22 D.-G. Wang, T. Qiu, W. Guo, Z. Liang, H. Tabassum, D. Xia and R. Zou, *Energy Environ. Sci.*, 2021, **14**, 688.
23 Z. Wang, S. Zhang, Y. Chen, Z. Zhang and S. Ma, *Chem. Soc. Rev.*, 2020, **49**, 708.
24 X. Zhao, P. Pachfule and A. Thomas, *Chem. Soc. Rev.*, 2021, **50**, 6871.
25 X. Han, C. Yuan, B. Hou, L. Liu, H. Li, Y. Liu and Y. Cui, *Chem. Soc. Rev.*, 2020, **49**, 6248.
26 N. Keller and T. Bein, *Chem. Soc. Rev.*, 2021, **50**, 1813.
27 Z. Guo, Y. Zhang, Y. Dong, J. Li, S. Li, P. Shao, X. Feng and B. Wang, *J. Am. Chem. Soc.*, 2019, **141**, 1923.
28 Y. Xu, P. Cai, K. Chen, Q. Chen, Z. Wen and L. Chen, *Angew. Chem., Int. Ed.*, 2023, **62**, e202215584.
29 Z. Liu, K. Zhang, G. Huang, B. Xu, Y.-l. Hong, X. Wu, Y. Nishiyama, S. Horike, G. Zhang and S. Kitagawa, *Angew. Chem., Int. Ed.*, 2022, **61**, e202110695.
30 W. Gong, Y. Ouyang, S. Guo, Y. Xiao, Q. Zeng, D. Li, Y. Xie, Q. Zhang and S. Huang, *Angew. Chem., Int. Ed.*, 2023, **62**, e202302505.
31 M. J. Strauss, I. Hwang, A. M. Evans, A. Natraj, X. Aguilar-Enriquez, I. Castano, E. K. Roesner, J. W. Choi and W. R. Dichtel, *J. Am. Chem. Soc.*, 2021, **143**, 17655.
32 G. Zhang, Y.-l. Hong, Y. Nishiyama, S. Bai, S. Kitagawa and S. Horike, *J. Am. Chem. Soc.*, 2019, **141**, 1227.
33 Y. Yan, Z. Liu, T. Wan, W. Li, Z. Qiu, C. Chi, C. Huangfu, G. Wang, B. Qi, Y. Yan, T. Wei and Z. Fan, *Nat. Commun.*, 2023, **14**, 3066.
34 H. Chen, H. Tu, C. Hu, Y. Liu, D. Dong, Y. Sun, Y. Dai, S. Wang, H. Qian, Z. Lin and L. Chen, *J. Am. Chem. Soc.*, 2018, **140**, 896.
35 Z. Li, Z.-W. Liu, Z. Li, T.-X. Wang, F. Zhao, X. Ding, W. Feng and B.-H. Han, *Adv. Funct. Mater.*, 2020, **30**, 1909267.
36 Y. Hu, N. Dunlap, S. Wan, S. Lu, S. Huang, I. Sellinger, M. Ortiz, Y. Jin, S.-h. Lee and W. Zhang, *J. Am. Chem. Soc.*, 2019, **141**, 7518.
37 K. Jeong, S. Park, G. Y. Jung, S. H. Kim, Y.-H. Lee, S. K. Kwak and S.-Y. Lee, *J. Am. Chem. Soc.*, 2019, **141**, 5880.
38 X. Li, Q. Hou, W. Huang, H.-S. Xu, X. Wang, W. Yu, R. Li, K. Zhang, L. Wang, Z. Chen, K. Xie and K. P. Loh, *ACS Energy Lett.*, 2020, **5**, 3498.
39 Q. Xu, S. Tao, Q. Jiang and D. Jiang, *J. Am. Chem. Soc.*, 2018, **140**, 7429.
40 Q. Xu, S. Tao, Q. Jiang and D. Jiang, *Angew. Chem., Int. Ed.*, 2020, **59**, 4557.
41 T. W. Kang, J.-H. Lee, J. Lee, J. H. Park, J.-H. Shin, J.-M. Ju, H. Lee, S. U. Lee and J.-H. Kim, *Adv. Mater.*, 2023, **35**, 2301308.
42 J. N. Chazalviel, *Phys. Rev. A: At., Mol., Opt. Phys.*, 1990, **42**, 7355.
43 X. Zhang, A. Wang, X. Liu and J. Luo, *Acc. Chem. Res.*, 2019, **52**, 3223.
44 H. Zhang, C. Li, M. Piszcz, E. Coya, T. Rojo, L. M. Rodriguez-Martinez, M. Armand and Z. Zhou, *Chem. Soc. Rev.*, 2017, **46**, 797.
45 X. He, J. M. Larson, H. A. Bechtel and R. Kostecki, *Nat. Commun.*, 2022, **13**, 1398.
46 P. J. Waller, S. J. Lyle, T. M. Osborn Popp, C. S. Diercks, J. A. Reimer and O. M. Yaghi, *J. Am. Chem. Soc.*, 2016, **138**, 15519.
47 Z.-F. Pang, S.-Q. Xu, T.-Y. Zhou, R.-R. Liang, T.-G. Zhan and X. Zhao, *J. Am. Chem. Soc.*, 2016, **138**, 4710.
48 J. Dong, X. Li, S. B. Peh, Y. D. Yuan, Y. Wang, D. Ji, S. Peng, G. Liu, S. Ying, D. Yuan, J. Jiang, S. Ramakrishna and D. Zhao, *Chem. Mater.*, 2019, **31**, 146.
49 Y. An, X. Han, Y. Liu, A. Azhar, J. Na, A. K. Nanjundan, S. Wang, J. Yu and Y. Yamauchi, *Small*, 2022, **18**, 2103617.
50 Y. Xia, T. Fujieda, K. Tatsumi, P. P. Prosini and T. Sakai, *J. Power Sources*, 2001, **92**, 234.
51 J. Qiu, X. Liu, R. Chen, Q. Li, Y. Wang, P. Chen, L. Gan, S.-J. Lee, D. Nordlund, Y. Liu, X. Yu, X. Bai, H. Li and L. Chen, *Adv. Funct. Mater.*, 2020, **30**, 1909392.
52 X. Yang, M. Jiang, X. Gao, D. Bao, Q. Sun, N. Holmes, H. Duan, S. Mukherjee, K. Adair, C. Zhao, J. Liang, W. Li, J. Li, Y. Liu, H. Huang, L. Zhang, S. Lu, Q. Lu, R. Li, C. V. Singh and X. Sun, *Energy Environ. Sci.*, 2020, **13**, 1318.
53 Y. Liu, Y. Zhao, W. Lu, L. Sun, L. Lin, M. Zheng, X. Sun and H. Xie, *Nano Energy*, 2021, **88**, 106205.
54 J. Seo, G.-H. Lee, J. Hur, M.-C. Sung, J.-H. Seo and D.-W. Kim, *Adv. Energy Mater.*, 2021, **11**, 2102583.
55 H. Li, R. Meng, C. Ye, A. Tadich, W. Hua, Q. Gu, B. Johannessen, X. Chen, K. Davey and S.-Z. Qiao, *Nat. Nanotechnol.*, 2024, **19**, 792–799.